

The ultraviolet study of B[e] stars: evidence for pulsations, LBV-type variations, and processes in envelope

I. Krtičková^{*} and J. Krtička

Department of Theoretical Physics and Astrophysics, Masaryk University, Kotlářská 2, CZ-611 37 Brno, Czech Republic

Accepted XXX. Received YYY; in original form ZZZ

ABSTRACT

Stars with B[e] phenomenon comprise a very diverse group of objects in a different evolutionary status. These objects show common spectral characteristics, including presence of Balmer lines in emission, forbidden lines, and strong infrared excess due to the dust. The observations of emission lines indicate the illumination by ultraviolet ionizing source, which is a key part to understand the elusive nature of these objects. We study the ultraviolet variability of many B[e] stars to specify the geometry of the circumstellar environment and its variability. We analyse massive hot B[e] stars from our Galaxy and from Magellanic Clouds. We study the ultraviolet broad-band variability derived from the flux-calibrated data. We determine variations of individual lines and its correlation with the total flux variability. We detected variability of the spectral energy distribution and of the line profiles. The variability has several sources of origin, including the light absorption by the disk, pulsations, LBV-type variations, and eclipses in the case of binaries. The stellar radiation of most of B[e] stars is heavily obscured by circumstellar material. This suggests that the circumstellar material is not present only in the disk but also above its plane. The flux and line variability is consistent with a two-component model of circumstellar environment composed of the dense disk and ionized envelope. The observations of B[e] supergiants show that many of these stars have nearly the same luminosity of about $1.9 \times 10^5 L_{\odot}$ and similar effective temperature.

Key words: stars: early-type – stars: emission-line, Be – stars: variables: general – stars: winds, outflows – stars: oscillations

1 INTRODUCTION

B[e] stars form a very diverse group of stars that share common spectroscopic properties, however their astrophysical nature is very different. Among the typical spectroscopic properties of B[e] stars belong strong Balmer lines in emission, presence of low excitation permitted emission lines as well as forbidden emission lines, and infrared excess (Allen & Swings 1976). Despite their spectral similarities, the astrophysical nature of stars showing B[e] phenomenon is diverse. The group of B[e] stars contains stars in different evolutionary stages (pre-main sequence B[e] stars vs. B[e] supergiants), stars with different initial mass (massive B[e] supergiants vs. compact planetary nebulae), and binary status (including symbiotic binaries). Besides these classes of stars showing B[e] phenomenon summarized by Lamers et al. (1998) also presumably unevolved B[e] stars may appear (Miroshnichenko 2007).

The variability observed in the optical photometry (e.g., Sitko et al. 1994, de Winter & van den Ancker 1997, van Genderen & Sterken 1999) and spectroscopy (e.g., Borges Fernandes et al. 2012, Polster et al. 2012, Kučerová et al. 2013) indicates a possibility of ultraviolet (UV) variability. Although the UV flux variability was indeed found in some B[e] stars (Savage et al. 1978, Shore 1990, Sitko et al. 1994), there is no detailed systematic study of UV variability of B[e] stars according to our knowledge.

The study of UV variability of B[e] stars is especially relevant because hot stars emit most of their radiation in the UV domain. Consequently, the UV variability may shed some light on the elusive nature of many of these objects. The circumstellar environment of B[e] stars is combined from an ionized hot envelope and cool dusty material (Shore & Sanduleak 1983). While the presence of ionized envelope can be naturally explained by radiatively driven stellar wind, which is common in luminous stars of spectral type B (Vink et al. 2000, Crowther et al. 2006, Markova & Puls 2008), the origin of a cool dust containing envelope is unclear. The cool envelope is likely shaped in the form

^{*} E-mail: 15124@mail.muni.cz

of a disk (Zickgraf et al. 1985, Schulte-Ladbeck & Clayton 1993) whose inner parts may be relatively hot and shield the remaining cooler parts (e.g., Kraus & Lamers 2003, Zsargó et al. 2008).

The geometry of the circumstellar environment may therefore to some extent resemble classical Be stars (see Rivinius et al. 2013, for a review of Be phenomenon). Classical Be stars may contain a viscous disk that is fed as a result of angular momentum loss from near critically rotating star (Lee et al. 1991, Okazaki 2001, Krtiřka et al. 2011, Kurfürst et al. 2014). The origin of the disk is still a matter of debate in Be stars as well as in B[e] stars. The near critical rotation in these stars may possibly be induced either by evolutionary spin up (Granada et al. 2013) or by a binary interaction (Bogomazov & Tutukov 2009). The later hypothesis may be more likely in B[e] supergiants because the evolutionary models show strong decrease of the rotational velocity in the supergiant phase (Ekström et al. 2012).

The merger origin of B[e] stars was proposed by, e.g., Podsiadlowski (2010). The flow during such event is complex and may involve outflows as well as inflows (e.g., Pejcha et al. 2016). The merger scenario may be supported by the presence of extended envelopes that appear around some B[e] stars (e.g., HD 34664, Chu et al. 2003, HD 38489, Kastner et al. 2010). Some B[e] stars are spectroscopic binaries (e.g., Djurašević et al. 2008, Marchiano et al. 2012).

In the following paper, we analyse the archival IUE data available for B[e] stars to better understand the geometry of the circumstellar environment around these stars and to describe its variability in detail. Because the group of B[e] stars is very diverse, we focus on the stars that may share some common characteristics and exclude pre-main sequence stars, planetary nebulae, and symbiotic binaries from our analysis. We study mostly unevolved and evolved hot massive stars that display the B[e] phenomenon.

2 METHODS

We downloaded the far-UV 1150–1900 Å (SWP camera) and near-UV 2000–3300 Å (LWP and LWR cameras) low-dispersion large-aperture fluxes of B[e] stars from the INES database using the SPLAT-VO package (Draper 2014, Škoda et al. 2014). We selected only B[e] stars with multiple IUE observations that are suitable for the analysis of variability. The list of all used IUE observations is given in Appendix.

Motivated by the success in detection and modelling of the flux variability of chemically peculiar stars from IUE spectra (e.g., Krtiřka et al. 2012, Krtiřka et al. 2015), we selected the same approach to study the variability of B[e] stars. We constructed the broad-band fluxes

$$F_c = \int_0^{\infty} \phi_c(\lambda) F(\lambda) d\lambda \quad (1)$$

from the UV fluxes $F(\lambda)$ observed by IUE. Here $\phi_c(\lambda) = (\sqrt{\pi}\sigma)^{-1} \exp[-(\lambda - c)^2/\sigma^2]$ is a Gauss function centered on the wavelength c . The central wavelengths of individual Gauss filters were selected to describe the individual regions of UV spectra. We focused on the regions without strong emission lines. We selected $c = 1500$ Å to describe the flux in far-UV regions, $c = 2175$ Å which selects the flux in the

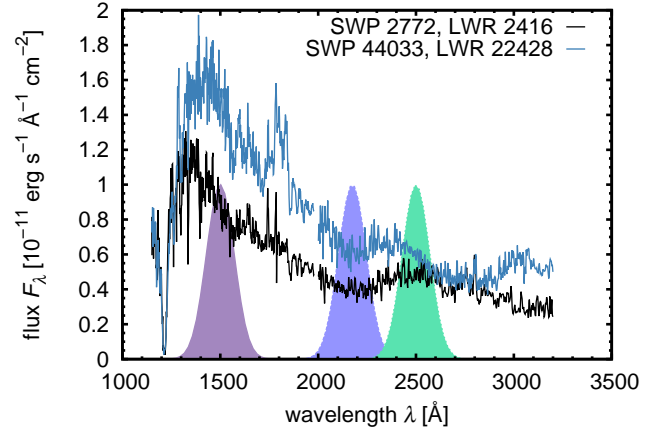


Figure 1. Example of the analysis of the broad-band variations of HD 45677. We plot the flux distribution for two different epochs (black and blue solid curves). Overplotted are individual adopted bandpass filters (not to scale). The change of broad-band fluxes is about 60 % in fluxes F_{1500} and F_{2175} and about 20 % in F_{2500} (see Table A8).

region of carbon opacity bump, and $c = 2500$ Å for near-UV region (see Fig. 1). The filters centered on different wavelength regions allow us to study the variations of temperature. Moreover, the regions of $c = 1500$ Å and $c = 2500$ Å are affected by the interstellar reddening by nearly the same amount (Fitzpatrick & Massa 2007). We selected $\sigma = 100$ Å to cover a broader region of the stellar flux distribution. However, our tests showed that the selection of central wavelengths and the dispersion does not significantly affect final results. The variations are plotted as a function of modified Julian date (MJD), $\text{MJD} = \text{JD} - 2\,400\,000$. The derived values together with their mean uncertainties (in the same units) are given also in Tables A1–A13. We used our results for the comparison of individual fluxes and for the study of general relationships between them.

The emission lines in the spectra of B[e] stars also clearly show variability (e.g., Sanduleak 1978, Kučerová et al. 2013). However, their study is more problematic, because there is no clear continuum in UV region, and the true continuum may lie significantly above the anticipated level. To overcome this problem, we constructed a pseudocontinuum in each spectrum and subtracted the pseudocontinuum flux from observed flux to derive the total flux in individual lines (see Fig. 2). The pseudocontinuum was created by hand using the SPLAT-VO¹ package taking into account the flux distribution of stars without B[e] phenomenon. We used the spline function to connect the points corresponding to the pseudocontinuum. In other words, a similar procedure is typically applied as when normalizing a spectrum. To describe the variations of the emission and absorption lines as a whole, we integrated the flux above and below the pseudocontinuum in the region 1250–1900 Å to derive the total flux in the emission lines F_{em} and line absorption F_{abs} as shown in Fig. 2. The fluxes in individual strong lines and the total line fluxes are plotted in graphs

¹ <http://star-www.dur.ac.uk/~pdraper/splat/splat-vo/>

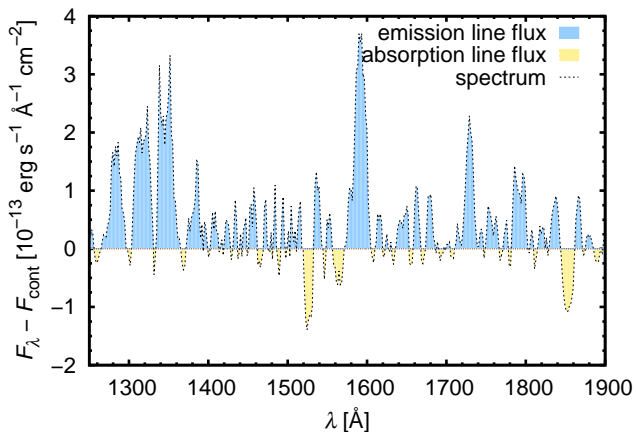


Figure 2. Example of the analysis of the line spectrum of HD 87643 (SWP 46913). The dashed line denotes the observed spectrum from which the pseudocontinuum was subtracted. The total emission line flux is the total flux above the zero (blue shaded area) and the total line absorption is the total flux below zero (yellow shaded area).

and also listed in Tables A1–A13. The uncertainties are given in the same units as individual fluxes.

During the construction of the pseudocontinuum, we focused our attention to a precise and homogeneous processing of all spectra. The repeated processing of selected spectra showed that we are able to reliably reproduce the derived results. Consequently, the line fluxes F_{em} and F_{abs} reflect the changes in the spectral properties of individual stars and enable the mutual comparison between studied stars. Moreover, the comparison with literature data shows that our emission line fluxes agree typically within 10–20% with that given in Shore & Sanduleak (1983) for HD 38489 (see Table A7) and in Shore et al. (1987) for LHA 115-S 18 (Table A1).

We also tested the dependence of the flux on the position angle of the slit to reveal large nebula around the star or nearby stellar object. We have not detected any such dependence for all stars except one. We found the dependence of the flux on the position angle for LHA 115-S 18, however, we interpret this dependence as coincidental.

Our additional aim was the determination of the temperature of the stellar envelope. We fitted the observed spectra by theoretical spectral energy distribution. We selected the spectra for which nearly simultaneous observations are available in far-UV and near-UV regions. The spectra were fitted by ATLAS9 fluxes² (Kurucz 2005, Castelli 2005) calculated assuming LTE, which cover the studied temperature interval. We selected solar chemical composition for the Galactic stars and $[M/H] = -0.5$ for stars from the Magellanic Clouds. The spectra were attenuated by the extinction curve $k(\lambda - V)$ of Fitzpatrick & Massa (2007),

$$F(\lambda) = F_0(\lambda) 10^{-\alpha k(\lambda-V)}, \quad (2)$$

where $F_0(\lambda)$ is unattenuated flux and α is a free parameter of the fit. The other fit parameters are the model effective

² <http://www.oact.inaf.it/castelli/>

Table 1. Basic properties and temperatures T_{UV} (see Sect. 2) of studied stars. Here “sg” denotes supergiant, “b” binary, “eb” eclipsing binary and “H” Herbig Ae/Be star.

Star	Location	Type	T_{UV} [K]
LHA 115-S 18 (AzV 154)	SMC		
LHA 115-S 65 (Sk 193)	SMC	sg	9100 ± 100
LHA 120-S 12 (Sk -67 23)	LMC	sg	18800 ± 300
HD 34664 (LHA 120-S 22)	LMC	sg	$9500 - 10500$
HD 37974 (LHA 120-S 127)	LMC	sg	12800 ± 400
HD 38489 (LHA 120-S 134)	LMC	sg	16900 ± 1000
HD 45677 (FS CMa)	Gal.		$14100 - 16300$
HD 50138 (V743 Mon)	Gal.		11700 ± 200
HD 87643 (V640 Car)	Gal.	b	$10900 - 11700$
HD 94878 (GG Car)	Gal.	eb	27800 ± 700
HD 100546 (KR Mus)	Gal.	H	12000 ± 200
HD 169515 (RY Sct)	Gal.	eb	35000 ± 1000

temperature and surface gravity. For normal stars without circumstellar envelope, the model effective temperature corresponding to the best fit of the UV flux distribution is equal to the effective temperature of the star. For the stars with opaque circumstellar environment, the stellar effective temperature may be different, and consequently we denote the temperature corresponding to the best fit of UV spectra as T_{UV} . This temperature corresponds to the temperature of the circumstellar envelope. Because the fluxes are rather insensitive to the surface gravity, we do not provide its final value. B[e] stars typically show infrared excess due to the dust. Consequently, part of the dust absorption accounted by Eq. (2) may originate in circumstellar environment of given star. However, because infrared dust emission traces large volumes of the circumstellar medium, while the dust absorption is given just by the dust particles intersecting the line of sight, we expect that the interstellar contribution may dominate in Eq. (2). Anyway, both contributions are accounted for in Eq. (2) because our approach does not assume any particular spatial distribution of the dust. We fitted just the normalized fluxes.

3 UV VARIABILITY OF INDIVIDUAL STARS

We searched the IUE archive for the observations of B[e] stars with multiple IUE spectra. Basic properties of studied stars are given in Appendix A and are summarized in Table 1 including the temperature T_{UV} derived from the spectral energy distribution fit. We provide range of temperatures for the stars that show variability of T_{UV} . We have not found any clear variations of the dust absorption parameter α Eq. (2) in any star.

3.1 LHA 115-S 18

The star LHA 115-S 18 shows a prominent UV flux variability (Fig. A1). This variability is caused mostly by emission lines, whereas the continuum varies only weakly (Shore et al. 1987). In accordance with Shore et al. (1987), we detected line variability in N V 1245 Å, O I 1302 Å, C IV 1550 Å, and He II 1640 Å lines (Table A1). The total emission line flux

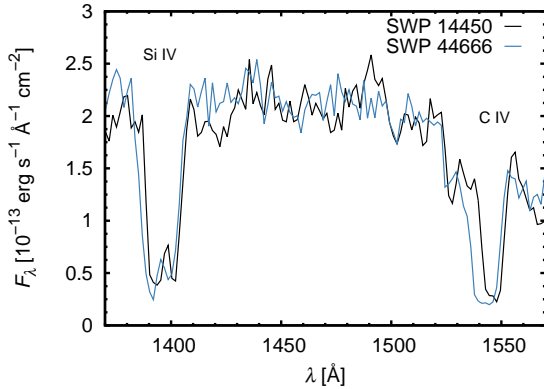


Figure 3. Variations of LHA 120-S 12 wind line profiles.

and the total line absorption flux vary (Table A1). The typical timescale of the variability (about four years) is longer than the most prominent cycle of optical variations, which is about 440 days (Clark et al. 2013). We have not fitted the spectrum of this star, because the continuum is relatively weak.

3.2 LHA 115-S 65

All IUE observations of LHA 115-S 65 were obtained in two different epochs. Consequently, we calculated just mean values of individual fluxes in both epochs (Table A3). While the fluxes at 1500 Å and 2500 Å do not change within the errors, there may be a decrease of the flux at 2175 Å. This may indicate increased dust absorption by intervening circumstellar material.

3.3 LHA 120-S 12

The IUE observations of LHA 120-S 12 are scarce. However, the wind line profiles show variability. The most prominent is the increase of the wind terminal velocity apparent in the C IV 1548 Å line profile from $1400 \pm 200 \text{ km s}^{-1}$ to $2300 \pm 200 \text{ km s}^{-1}$ (see Fig. 3) during roughly 11 years. Similar changes are present also in Si IV 1393 Å line, albeit with a lesser extent. While the total line absorption and the total emission line flux do not change substantially, the fluxes in Si IV doublet and in C IV line increase (Table A4). If the fitted temperature $T_{UV} = 18800 \pm 300 \text{ K}$ corresponds to the effective temperature of the star, then the change of the wind terminal velocity can be explained as a result of bistability (Pauldrach & Puls 1990). This effect appears close to $T_{\text{eff}} \approx 20000 \text{ K}$ and leads to the modification of the wind terminal velocity (Lamers et al. 1995, Crowther et al. 2006) and possibly also of the mass-loss rate as a result of sensitivity of wind ionization to the effective temperature of the star (Vink et al. 1999, Petrov et al. 2016).

3.4 HD 34664

The flux variations of HD 34664 in Fig. 4 show a strong decrease of the flux between MJD 45000 and 48000 detected by Shore (1990). The decrease of the flux is stronger in far-UV band centered at 1500 Å than in near-UV bands

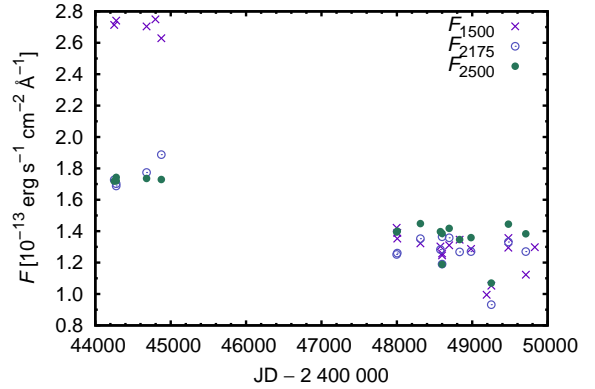


Figure 4. Variation of HD 34664 broad-band fluxes with time.

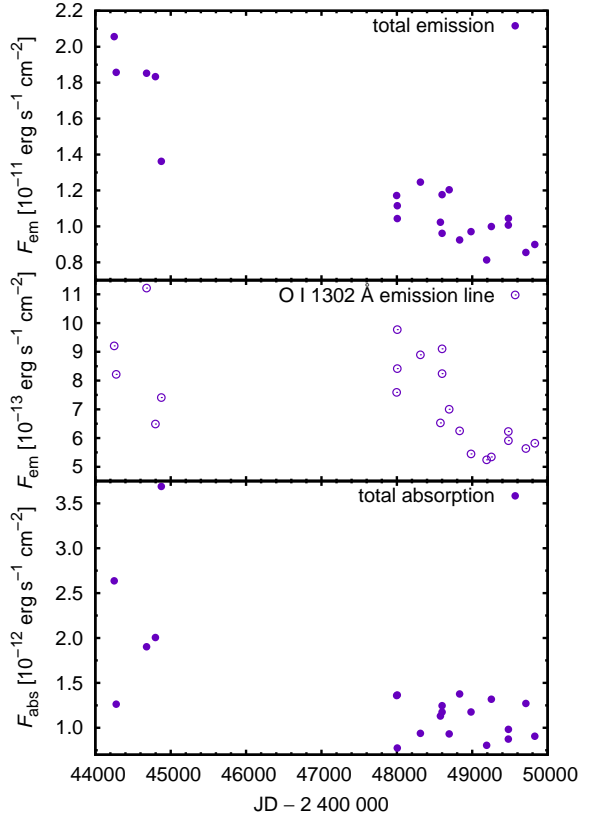


Figure 5. Variation of HD 34664 total emission line flux (*upper panel*), O I 1302 Å emission line flux (*middle panel*), and the total line absorption (*lower panel*) with time.

centered at 2175 Å and 2500 Å. This shows that the most likely cause of the light variability is the change of the effective temperature of the star. Such changes, which are typical for LBV S Doradus variables, were detected in HD 34664 by van Genderen & Sterken (1999) and Sterken (2011) from optical data. In accordance with this interpretation, van Genderen & Sterken (1999) detected optical reddening of this star over roughly the same period covered by IUE data.

The variations of the total absorption and the total emission line fluxes in Fig. 5 show linear decrease in both

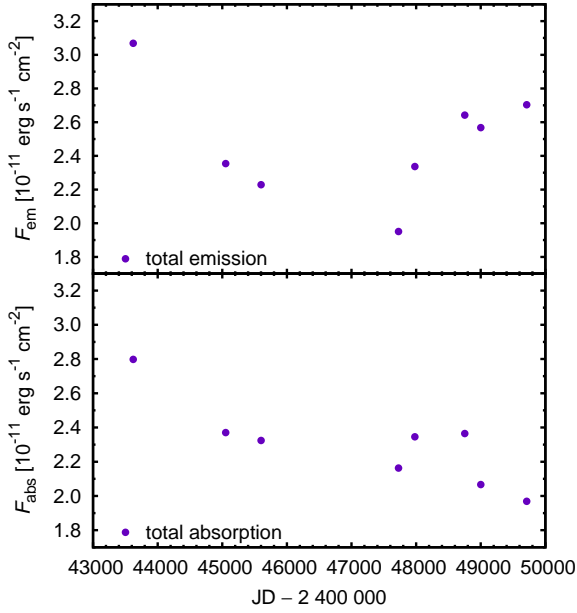


Figure 6. Variation of HD 37974 total emission line flux (*upper panel*) and the total line absorption (*lower panel*) with time.

cases followed by the period of constant flux in the case of the line absorption. These variations of the total line fluxes correspond to the decrease of the effective temperature of the star and are modified by the circumstellar envelope. The most intriguing is the decrease of the emission line flux even during the period of the constant flux after MJD 48 000 (Fig. 5, middle panel). This may indicate that the regions of origin of emission and absorption lines are different.

The temperature fitting yields a slow decrease from $T_{UV} = 10\,500 \pm 200$ K to $T_{UV} = 9\,500 \pm 100$ K. This decrease corresponds to broad-band flux and emission line flux variations.

3.5 HD 37974

The flux variations of HD 37974 in Fig. A2 can be interpreted as the flux decrease during MJD 43 000 – 46 000 and slight brightening in the period MJD 48 000 – 50 000. Additional variations may be connected with complex long-term (hundreds of days) and short-time (tens of days) optical light variability (van Genderen & Sterken 2002).

The variations of O I 1302 Å emission line in Fig. A2 as well as the total emission line flux in Fig. 6 show similar trends as F_{1500} fluxes, that is decrease during MJD 43 000 – 46 000 and increase of the later phases. The total line absorption decreased during the whole observational period (Fig. 6).

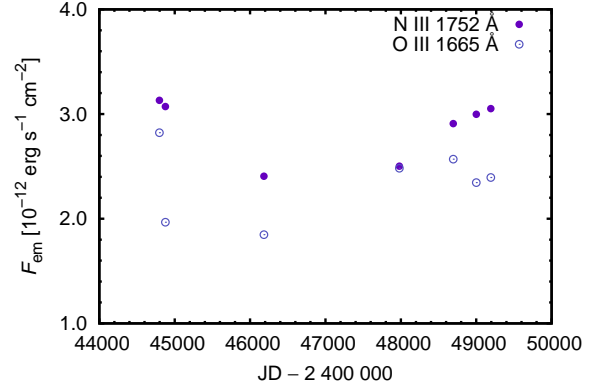


Figure 7. Variation of HD 38489 fluxes in emission lines O III 1665 Å and N III 1752 Å lines with time.

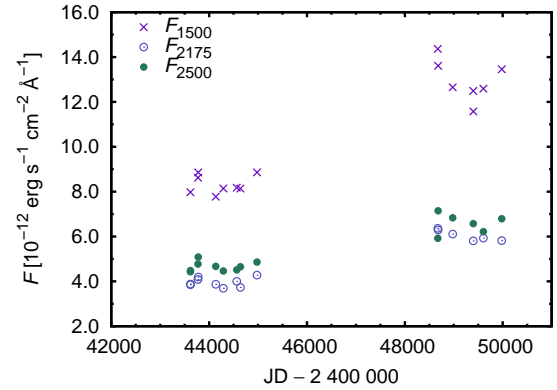


Figure 8. Variation of HD 45677 broad-band fluxes with time.

3.6 HD 38489

The IUE spectra of HD 38489 secured between MJD 44 800 – 49 200 show nearly constant flux³ (Shore & Sanduleak 1983) with dispersion of about 2%. Also the optical observations do not show any strong variability (Zickgraf et al. 1986). Despite this, the star shows emission line variability. He II 1640 Å (Shore & Sanduleak 1983) emission line flux increased during the period of IUE observation (Table A7). On the other hand, O III line at 1665 Å and N III line at 1752 Å show decrease followed by increase of the flux (see Fig. 7). The similarity of O III and N III emission line flux variations supports the idea that these lines originate in the same region, which is different from the region where He II line originates (Shore & Sanduleak 1983). Neither the total emission nor line absorption show a strong variability as a result of differing trends in the variability of individual lines.

3.7 HD 45677

The UV flux variations of HD 45677 in Fig. 8, which show increase of the flux from MJD of about 44 000 to 48 000, are correlated with visual light variations (Sitko et al. 1994).

³ The observations at about MJD=49 250 show flux dip, but we regard this just as an instrumental feature, because a similar dip is present in observations of HD 34664 (see Fig. 4).

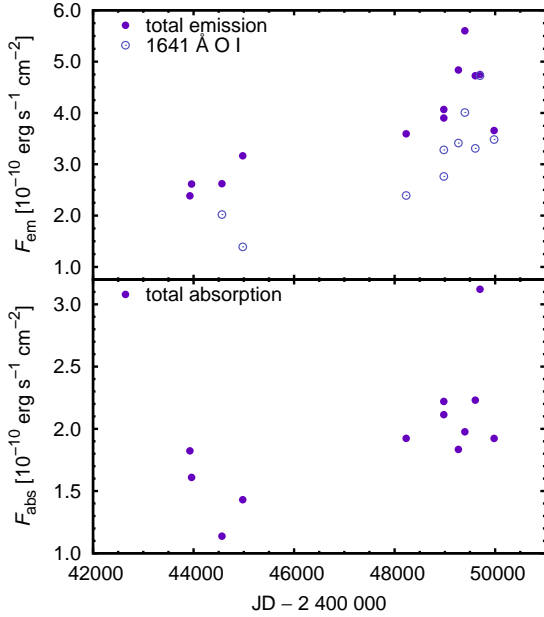


Figure 9. Variation of HD 45677 fluxes in emission (*upper panel*) and absorption (*lower panel*) lines with time. The emission flux in 1641 Å O I line was artificially multiplied by ten to get the common scale of the graph.

Slightly decreasing trend between MJD 48 000 – 50 000 may be connected with regress from the visual light maximum that appeared at about MJD 48 700 (Sitko et al. 1994). The maximum is visible also in the Hipparcos data (ESA 1997).

The total emission flux, 1641 Å O I emission line flux (see Fig. 9), and the 1745 Å N I (Sitko & Savage 1980, Brown et al. 1995) line flux show a similar behaviour as the total absorption and broad-band fluxes. This indicates that the corresponding processes are connected.

The temperature T_{UV} decreased from about $16\,300 \pm 500$ K in MJD 43 000 – 45 000 to $14\,100 \pm 300$ K in MJD 48 000 – 49 000. The fluxes do not change significantly below about 1300 Å, but significantly increase above 1300 Å in later epochs. Moreover, the flux maximum shifts from 1300 Å to about 1400 Å, causing the mentioned decrease of T_{UV} .

3.8 HD 50138

The IUE observations of HD 50138 cover two epochs with MJD of about 43 800 – 45 000 and 48 600 – 49 800. The stellar flux systematically decreased during MJD 43 800 – 45 000 in all bands studied here, but the short-term variations are also significant during that epoch (see Fig. 10). These short term variations are apparent in the Hipparcos photometry (ESA 1997) and possibly also in the visual photometry (Halbedel 1991). The flux reached original level during MJD 48 600 – 49 800. The long-term variations could be probably explained by increasing obscuration by the matter expelled during outburst (Hutsemekers 1985), which was already dispersed in the second epoch.

We used Period04 (Lenz & Breger 2005) to analyse the F_{2175} and F_{2500} data in the epoch MJD 49 400 – 49 800 yielding the detection of the period 1.194 ± 0.006 d. A similar frequency is present also in the F_{1500} data albeit with much

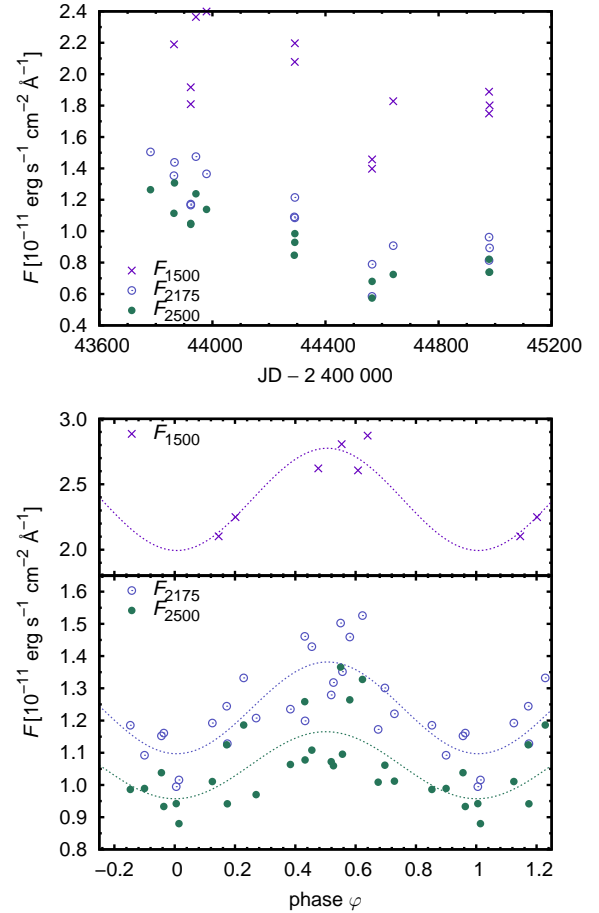


Figure 10. Variation of HD 50138 broad-band fluxes. *Upper panel:* Long-term variations during MJD 43 800 – 45 000. *Bottom panel:* Periodic variations during MJD 49 400 – 49 800 plotted with ephemeris $JD=2\,449\,701.18 \pm 1.194E$.

larger uncertainty. All variations can be nicely fitted by simple sinusoids (see Fig. 10). We have checked the data from MJD 43 800 – 45 000 and data from Hipparcos (taken in MJD 47 900 – 49 100) and we have not found any reasonable periodicity.

The total emission and absorption line fluxes also show strong variations for MJD 43 800 – 45 000 (see Fig. A3). The inspection of the total line absorption in the epoch MJD 49 400 – 49 800 also shows possible periodicity, but with relatively large scatter. However, the total emission line fluxes show steady increase for MJD 49 400 – 49 800 when the periodical photometric variations are detected.

The stochastic variations during MJD 43 800 – 45 000 may be the consequence of the outburst that appeared in 1978–1979 (Hutsemekers 1985). Borges Fernandes et al. (2012) attributed the detected photospheric variations to pulsations. If this model is correct, then the fact that the pulsations are detectable only during the epoch when the star does not show stochastic variations likely means that either the pulsations are triggered by stochastic variations or are hidden in these variations. Kraus et al. (2015) suggested that pulsations in a blue supergiant 55 Cygni can lead to phases of enhanced mass loss. In HD 50138, this could be possibly connected to the increase of the total

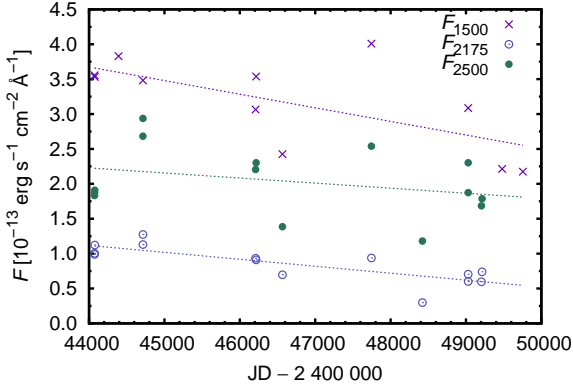


Figure 11. Variation of HD 87643 broad-band fluxes with time. Lines denote linear fit to individual broad-band fluxes.

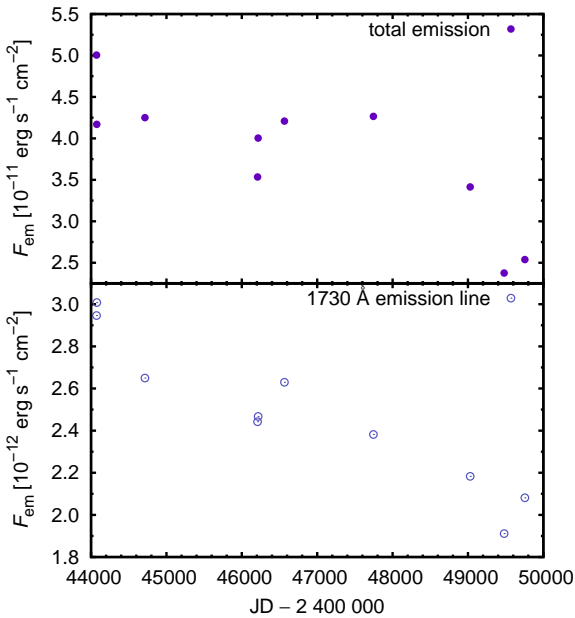


Figure 12. Variation of HD 87643 total emission line flux (*upper panel*) and the flux in the emission line at 1730 Å (*lower panel*).

emission line flux (Fig. A3). The pulsational period is close to that found in main-sequence stars with similar spectral type (Diago et al. 2009, Neiner et al. 2009) indicating that HD 50138 is still main-sequence star (in agreement with Borges Fernandes et al. 2009).

For $\text{MJD} > 49\,000$ the observations possibly evince the phase variability of T_{UV} from about $11\,800 \pm 200$ K to about $11\,400 \pm 200$ K. The region close to the Ly α line shows a relatively broad (at about 1150 – 1250 Å) flux minimum, which is connected with low T_{UV} .

3.9 HD 87643

The IUE observations of HD 87643 in Fig. 11 covering the period of $\text{MJD} 44\,000 - 50\,000$ show an overall decrease of the flux with possibly additional stochastic variations. We fitted the flux variations with linear function $F_{\lambda}(\text{MJD}) = a_{\lambda}(\text{MJD} - \overline{\text{MJD}}) + b_{\lambda}$, where $\overline{\text{MJD}}$ is the mean

MJD for each observational set. The wavelength dependence of a_{λ} and b_{λ} can be explained by the variations of either dust absorption or temperature. The decrease of the broad-band fluxes is accompanied by the decrease of the total and 1730 Å emission line fluxes (see Fig. 12). A similar decrease appears in 1590 Å emission line flux. The total line absorption varies between $\text{MJD} 44\,000$ and $\text{MJD} 49\,800$ with the maximum roughly in the middle of the time interval and with the minima at the beginning and the end of the observational time period (Table A10).

The fitting of the flux reveals a possible increase of the T_{UV} during the studied period from about $10\,900 \pm 200$ K to $11\,700 \pm 800$ K.

3.10 HD 94878

Despite the binary nature of the object, HD 94878 does not show any clear periodicity of UV fluxes. Even the phase diagram based on the ephemeris of Marchiano et al. (2012) does not show any clear trend in any colour. This is probably connected with low amount of data and with the fact that the visual light variations show a large scatter (Gosset et al. 1984, van Leeuwen et al. 1998) possibly as a result of the intrinsic variability of a component. This component likely dominates in UV making the binary lightcurve undetectable. The broad-band photometry does not show any long-term variability in the studied time interval.

Despite the lack of clear flux variability, the absorption lines show variability which may be orbitally modulated. The C II 1335 Å (Brandi & Gosset 1987) line absorption is variable (see Table A11) with possible minimum around the phase 0.3 of Marchiano et al. (2012). On the other hand, the C IV absorption line at 1548 Å does not evince orbitally modulated variability. The total emission and absorption fluxes suggest variability (Table A11). The broad-band flux F_{2175} is relatively low compared to other fluxes, which is caused by the dust absorption.

3.11 HD 100546

The UV spectrum of HD 100546 does not show any clear flux variability. A small dispersion of UV flux of about 6% is consistent with small amplitude of optical variability (van den Ancker et al. 1998). There may be increase of the flux in the emission line at 1779 Å and the total emission line flux from $\text{MJD}=48\,000$ to $50\,000$ (Table A12). There may be also some variability in 1657 Å Fe II absorption line. Other absorption lines as C II 1335 Å and the total line absorption do not show any variability (Table A12).

3.12 HD 169515

The stellar spectral energy distribution of HD 169515 evince strong influence of the dust absorption on F_{2175} fluxes, which are by order of magnitude lower than F_{2500} fluxes. We have not detected any clear long term flux variability of this star, however, we are able to detect the 11.1 d orbital period (Kreiner 2004) from the 1500 Å and 2500 Å flux data.

The total emission and absorption fluxes do not show any strong phase dependence, but there may be long-term variations of the total fluxes. The decrease of the

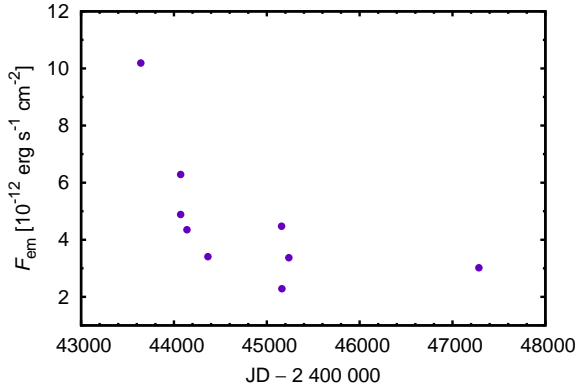


Figure 13. Variation of HD 169515 total emission line flux.

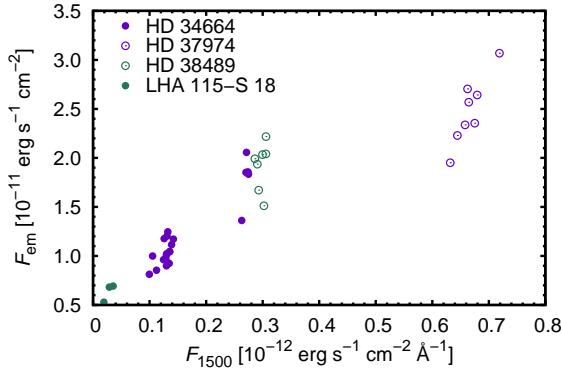


Figure 14. Relation between the far-UV broad band fluxes and the total emission line fluxes for the stars from the Magellanic Clouds.

total emission line flux during the observational period is shown in Fig. 13. The total line absorption displays slightly downward trend during the observational period. Individual lines show phase dependence. The Fe II absorption line at 1658 Å (Sahade et al. 2002) is the weakest during visual eclipses (using ephemeris of Kreiner 2004). We have not detected any phase variability of C IV emission lines at 1550 Å (Sahade et al. 2002), but all studied lines evince variability, which means Si IV 1402 Å emission line, C IV 1550 Å emission line, and Fe II 1658 Å absorption line (Table A13).

4 GENERAL RELATIONS BETWEEN INDIVIDUAL FLUXES

Fig. 14 shows that there is correlation between the far-UV broad band fluxes and the total emission line fluxes for the stars from the Magellanic Clouds. The emission line flux depends on the amount of ionizing radiation and therefore on the stellar effective temperature and radius. However, these parameters can not be the cause of the relationship in Fig. 14, because in limit of zero broad-band flux F_{1500} the emission line flux F_{em} does not approach zero. Consequently, it is more likely that the relationship results from geometrical reasons, i.e., from varying inclination or radius of the disk. The origin of continuum and some emission lines

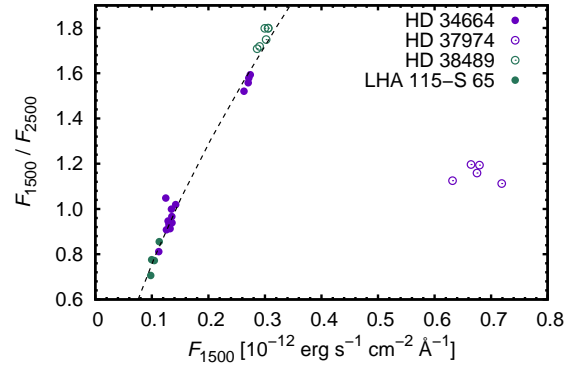


Figure 15. Relation between the far-UV broad band fluxes and the ratio of far-UV and near-UV broad band fluxes for the stars from the Magellanic Clouds. Dashed line denotes $F_{1500} \sim T_{\text{eff}}^4 F_{1500}/F_{2500}$ relation derived from ATLAS model atmospheres.

is different. Therefore, the relationship in Fig. 14 could be possibly explained assuming that with larger disk column density (or with higher disk inclination, i.e., for disks seen edge-on) the flux gets more absorbed and therefore F_{1500} becomes lower. However, some parts of the envelope are visible even for high inclinations or large disk radii, consequently, F_{em} is nonzero for very low F_{1500} . Because the amount of ionizing radiation depends mainly on the effective temperature, a relatively tight correlation of F_{1500} and F_{em} fluxes indicates that the supergiant B[e] stars in the Magellanic Clouds come from a relatively narrow range of the stellar parameters.

With exception of HD 37974, the ratio of far-UV and near-UV broad band fluxes for stars from the Magellanic Clouds depends on the far-UV flux (see Fig. 15). We have not included LHA 115-S 18 in the plot, because the star does not show a strong continuum. The variations in Fig. 15 show a tight linear trend for all stars except HD 37974 despite complicated flux variations in individual stars. The relation can be fitted using model atmospheres emergent fluxes f_{1500} and f_{2500} (Kurucz 2005) assuming constant luminosity of B[e] stars and variable UV temperature and radius R_{UV} , as $L \sim R_{UV}^2 T_{UV}^4$ or $R_{UV}^2 \sim T_{UV}^{-4}$ for constant L . From this follow relationships $f_{1500}/T_{UV}^4 \sim f_{1500}/f_{2500}$ or $f_{1500} \sim T_{UV}^4 f_{1500}/f_{2500}$ for the model atmosphere fluxes, or (multiplying by R_{UV}^2) $F_{1500} \sim F_{1500}/F_{2500}$. The flux f_{1500} in Fig. 15 was linearly scaled to fit the observed relation and T_{UV} is the effective temperature T_{eff} corresponding to model atmosphere flux. These results show that a large group of B[e] supergiants has the same luminosity of about $(1.9 \pm 0.4) \times 10^5 L_{\odot}$ from the model atmospheres, assuming the LMC distance 50 kpc (de Grijs et al. 2014), and correcting for mean extinction derived here. This can provide the possibility to reveal the origin of B[e] supergiant stars. Moreover, with a proper calibration, the relationship in Fig. 15 could be used for distance estimation.

Fig. 16 shows that there is not a clear correlation between the emission line flux and the ratio of F_{1500}/F_{2500} , which is a temperature indicator. The lack of correlation supports a general picture that the continuum flux observed

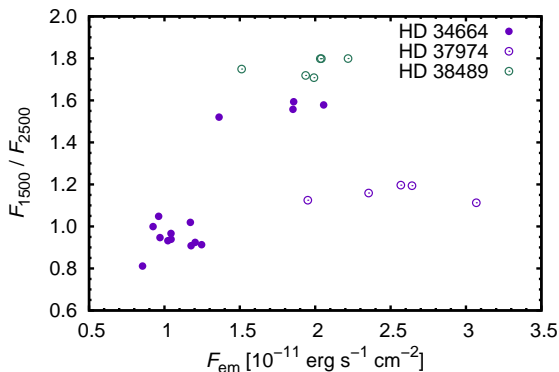


Figure 16. Relation between the total emission line flux and the ratio of far-UV and near-UV broad band fluxes for the stars from the Magellanic Clouds.

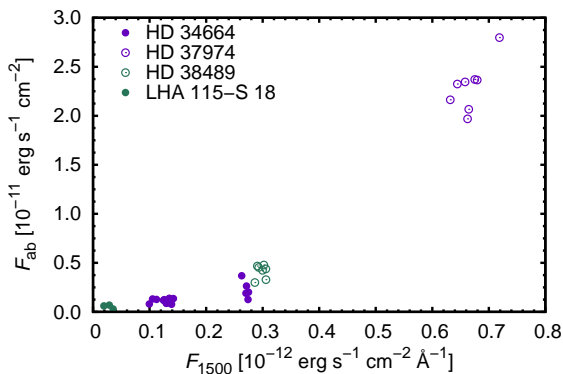


Figure 17. Relation between the broad-band flux at 1500 Å and the total line absorption for the stars from the Magellanic Clouds.

in the UV region does not originate in the stellar atmosphere.

The total line absorption is strongly correlated with the F_{1500} flux for the stars from the Magellanic Clouds (see Fig. 17). The F_{1500} flux increases with increasing temperature of the circumstellar envelope, consequently, from the nonlinearity of the relationship in Fig. 17 follows that the absorption lines become relatively stronger for higher temperature of the envelope.

5 DISCUSSION AND CONCLUSIONS

We studied the UV variability of B[e] stars in individual lines and in broad-band fluxes. From the observed flux distribution, we calculated the broad-band variations using artificial photometric filters centered on selected wavelengths. We evaluated the total emission and absorption line fluxes and studied their variability, which originates in the stellar envelope, disk, and the star alone. The observed spectral energy distributions were fitted with atmosphere flux attenuated by the dust absorption.

The UV domain provides wealth of information about the variability of B[e] stars. The multi-colour photometry centered ideally in the far-UV and near-UV regions is able

to detect long-term variability (in LHA 115-S 18, HD 37974, HD 45677, HD 50138, and HD 87643) and the S Doradus type variability (in the case of HD 34664). The detected eclipses in HD 169515 may help to constraint the nature of companions. Some stars also show irregular short-term variability (HD 94878). In HD 50138, we also detected pulsations, which are relatively rare among B[e] stars. The derived pulsation period in HD 50138 is 1.194 d. This is the first unambiguous detection of the pulsation and measurement of its period in this star. Some B[e] stars do not show any strong flux variability (LHA 115-S 65, HD 38489, and HD 100546).

The line variability is typically connected with the flux variability. In HD 34664 the decrease of the flux (and the estimated temperature) is correlated with the decrease of the line fluxes. A similar correlation is also found in HD 37974, HD 45677, and HD 87643. LHA 120-S 12 shows wind line profile variability that corresponds to the wind bistability jump. In HD 169515 we have found variability of absorption lines during the eclipses.

We found striking differences in the ratios of the total emission line flux to the total line absorption among studied stars perhaps as a consequence of envelope properties. The stars with high total emission line flux are LHA 115-S 18, LHA 115-S 65, HD 34664, HD 38489, HD 45677, HD 50138, HD 87643, and HD 169515. This group of stars shows the ratio of the total emission line flux to the total line absorption F_{em}/F_{ab} in the range 1.1–23.5. The predominance of emission line flux is typical for these stars. On the contrary, the stars LHA 120-S 12, HD 37974, HD 94878, and HD 100546 show low ratio of the total emission line flux to the total line absorption and the spectra evince more absorption lines than emission lines. We specify the ratio F_{em}/F_{ab} in the range 0.46–1.37 for these stars.

In many B[e] stars, the temperature obtained from the fitting of UV flux distribution is significantly lower than 20 kK. This is too low to cause a significant H α emission. This indicates that many B[e] stars are enshrouded by optically thick envelope, and a significant part of UV radiation does not originate on the surface of B[e] stars, but in their disk. The stellar radiation is heavily obscured in such stars, and the temperature derived from fitting corresponds to the temperature of the circumstellar environment. This conclusion is further supported by the relation between the broad-band fluxes and total emission line flux. Possibly, the absorbing material appears also above the disk.

The fitted amount of the dust absorption derived from the 2175 Å opacity bump does not vary with time in majority of stars. This indicates the interstellar origin of this feature in many stars.

The fluxes from the Magellanic Cloud stars show that many B[e] stars evince the same luminosity of about $1.9 \times 10^5 L_{\odot}$ and similar effective temperature. This indicates that the long-term broad-band variability of B[e] stars is most likely caused by the changes in the envelopes of these stars. Moreover, this puts strong constraints on the models of evolution of these stars and possibly establishes distance indicator.

ACKNOWLEDGEMENTS

This research was supported by GA R 16-01116S.

REFERENCES

- Allen D. A., Swings J. P., 1976, *A&A*, 47, 293
- Antokhina E. A., & Kumsiashvili M. I., 1999, *Astronomy Letters*, 25, 662
- Antonou V., Zezas A., Hatzidimitriou D., McDowell J. C., 2009, *ApJ*, 697, 1695
- Aret A., Kraus M., Muratore M. F., Borges Fernandes M., 2012, *MNRAS*, 423, 284
- Azzopardi M., Breysacher J., Muratorio G., 1981, *A&A*, 95, 191
- Bensammar S., Friedjung M., Muratorio G., Viotti R., 1983, *A&A*, 126, 427
- Bjorkman K. S., Miroshnichenko A. S., Bjorkman J. E., et al., 1998, *ApJ*, 509, 904
- Bogomazov A. I., Tutukov A. V. 2009, *Astronomy Reports*, 53, 214
- Borges Fernandes M., Kraus M., Chesneau O., et al., 2009, *A&A*, 508, 309
- Borges Fernandes M., Meilland A., Bendjoya P., et al., 2011, *A&A*, 528, A20
- Borges Fernandes M., Kraus M., Nickeler D. H., et al., 2012, *A&A*, 548, A13
- Brandi E., Gosset E. 1987, *A&AS*, 68, 283
- Brandi E., Gosset E., Swings J.-P., 1987, *A&A*, 175, 151
- Brown T. M., Buss R., Jr., Grady C., Bjorkman K., 1995, *ApJ*, 440, 865
- Castelli F., 2005, *Memorie della Societ Astronomica Italiana Supplement*, 8, 25
- Chu Y.-H., Chen C.-H. R., Danforth C., et al., 2003, *AJ*, 125, 2098
- Cidale L., Zorec J., Tringaniello L., 2001, *A&A*, 368, 160
- Clark J. S., Bartlett E. S., Coe M. J., et al., 2013, *A&A*, 560, A10
- Crampton D., 1971, *AJ*, 76, 260
- Crowther P. A., Lennon D. J., Walborn N. R., 2006, *A&A*, 446, 279
- de Freitas Pacheco J. A., Gilra D. P., Pottasch S. R., 1982, *A&A*, 108, 111
- de Grijs R., Wicker J. E., Bono G., 2014, *AJ*, 147, 122
- de Winter D., van den Ancker M. E., 1997, *A&AS*, 121, 275
- Diago P. D., Gutirrez-Soto J., Auvergne M., et al., 2009, *A&A*, 506, 125
- Djurašević G., Vince I., Atanacković O., 2008, *AJ*, 136, 767
- Draper P. W., 2014, *Astrophysics Source Code Library*, ascl:1402.007
- Ekstrm S., Georgy C., Eggenberger P., et al., 2012, *A&A*, 537, A146
- Ellerbroek L. E., Benisty M., Kraus S., et al., 2015, *A&A*, 573, A77
- ESA 1997, in *The Hipparcos and Tycho Catalogues*, ESA SP-1200, Noordwijk
- Fehrenbach C., 1971, *A&A*, 13, 437
- Fitzpatrick E. L., Massa D., 2007, *ApJ*, 663, 320
- Garufi A., Quanz S. P., Schmid H. M., et al., 2016, *A&A*, 588, A8
- Gnedin Y. N., Kiselev N. N., Pogodin M. A., Rosenbush A. E., Rosenbush V. K., 1992, *Soviet Astronomy Letters*, 18, 182
- Gosset E., Surdej J., Swings J. P., 1984, *A&AS*, 55, 411
- Grady C. A., Bjorkman K. S., Shepherd D., et al., 1993, *ApJ*, 415, L39
- Granada A., Ekstrm S., Georgy C., et al., 2013, *A&A*, 553, A25
- Greaves J., 2005, *Information Bulletin on Variable Stars*, 5699,
- Grundstrom E. D., Gies D. R., Hillwig T. C., et al., 2007, *ApJ*, 667, 505
- Halbedel E. M., 1991, *Information Bulletin on Variable Stars*, 3585, 1
- Hu J. Y., The P. S., de Winter D., 1989, *A&A*, 208, 213
- Hutsemekers D., 1985, *A&AS*, 60, 373
- Kastner J. H., Buchanan C. L., Sargent B., Forrest W. J., 2006, *ApJ*, 638, L29
- Kastner J. H., Buchanan C., Sahai R., Forrest W. J., Sargent B. A., 2010, *AJ*, 139, 1993
- Kreiner J. M., 2004, *Acta Astron.*, 54, 207
- Kraus M., Lamers H. J. G. L. M., 2003, *A&A*, 405, 165
- Kraus M., Borges Fernandes M., de Arajo F. X., 2010, *A&A*, 517, A30
- Kraus M., Oksala M. E., Nickeler D. H., et al., 2013, *A&A*, 549, A28
- Kraus M., Haucke M., Cidale L. S., et al., 2015, *A&A*, 581, A75
- Krťicka, J., Owocki S. P., Meynet G., 2011, *A&A*, 527, A84
- Krťicka J., Mikulšek Z., Luftinger T. et al., 2012, *A&A*, 537, A14
- Krťicka J., Mikulšek Z., Luftinger T., Jagelka M., 2015, *A&A*, 576, A82
- Kucerov B., Korakov D., Polster J., et al., 2013, *A&A*, 554, A143
- Kurfrst P., Feldmeier A., Krťicka J., 2014, *A&A*, 569, A23
- Kurucz R. L., 2005, *Memorie della Societ Astronomica Italiana Supplement*, 8, 14
- Lamers H. J. G. L. M., Zickgraf F.-J., de Winter D., Houziaux L., Zorec J., 1998, *A&A*, 340, 117
- Lanz T., Hubeny I., 2007, *ApJS*, 169, 83
- Lee U., Osaki Y., Saio H., 1991, *MNRAS*, 250, 432
- Lee C.-D., Chen W.-P., Liu S.-Y., 2016, *A&A*, 592, A130
- Lenz P., Breger M. 2005, *Communications in Asteroseismology*, 146, 53
- Liermann A., Kraus M., Schnurr O., Fernandes M. B., 2010, *MNRAS*, 408, L6
- Lindegren L., Lammers U., Bastian U., et al., 2016, *A&A*, 595, A4
- Lamers H. J. G. L. M., Snow T. P., Lindholm D. M., 1995, *ApJ*, 455, 269
- Magalhes A. M., 1992, *ApJ*, 398, 286
- Marchiano P., Brandi E., Muratore M. F., et al., 2012, *A&A*, 540, A91
- Markova N., Puls J. 2008, *A&A*, 478, 823
- McGregor P. J., Hyland A. R., Hillier D. J., 1988, *ApJ*, 334, 639
- Men’shchikov A. B., Miroshnichenko A. S., 2005, *A&A*, 443, 211
- Millour F., Chesneau O., Borges Fernandes M., et al., 2009, *A&A*, 507, 317
- Miroshnichenko A. S. 2007, *ApJ*, 667, 497
- Neiner C., Gutirrez-Soto J., Baudin F., et al., 2009, *A&A*, 506, 143
- Okazaki A. T., 2001, *PASJ*, 53, 119
- Oksala M. E., Kraus M., Cidale L. S., Muratore M. F., Borges Fernandes M., 2013, *A&A*, 558, A17
- Oudmaijer R. D., Proga D., Drew J. E., de Winter D., 1998, *MNRAS*, 300, 170
- Patel M., Oudmaijer R. D., Vink J. S., Mottram J. C., Davies B., 2006, *MNRAS*, 373, 1641
- Pauldrach A. W. A., Puls J. 1990, *A&A* 237, 409
- Pereyra A., de Arajo F. X., Magalhes A. M., Borges Fernandes M., Domiciano de Souza A., 2009, *A&A*, 508, 1337
- Petrov B., Vink J. S., Grfener G., 2016, *MNRAS*, 458, 1999
- Podsiadlowski P., 2010, *New Astron. Rev.*, 54, 39
- Polster J., Korakov D., Votruba V., et al., 2012, *A&A*, 542, A57
- Ponomareva G. A., 1981, *Soviet Astronomy Letters*, 7, 414
- Pejcha O., Metzger B. D., Tomida K., 2016, *MNRAS*, 461, 2527
- Rivinius T., Carciofi A. C., Martayan C., 2013, *A&ARv*, 21, 69
- Sahade J., Brandi E., Fontenla J. M., 1984, *A&AS*, 56, 17
- Sahade J., West R. M., Skul’sky M. Y., 2002, *Rev. Mex. Astron. Astrofis.*, 38, 259

- Sanduleak N., 1978, *Information Bulletin on Variable Stars*, 1389, 1
- Savage B. D., Wesselius P. R., Swings J. P., The P. S., 1978, *ApJ*, 224, 149
- Schulte-Ladbeck R. E., Shepherd D. S., Nordsieck K. H., et al., 1992, *ApJ*, 401, L105
- Schulte-Ladbeck R. E., Clayton G. C., 1993, *AJ*, 106, 790
- Shore S. N., 1990, *IAU Circ.*, 5005, 1
- Shore S. N., Sanduleak N., 1983, *ApJ*, 273, 177
- Shore S. N., Sanduleak N., 1984, *ApJS*, 55, 1
- Shore S. N., Sanduleak N., Allen D. A., 1987, *A&A*, 176, 59
- Sitko M. L., Savage B. D., 1980, *ApJ*, 237, 82
- Sitko M. L., Meade M. R., Savage B. D., 1981, *ApJ*, 246, 161
- Sitko M. L., Halbedel E. M., Lawrence G. F., Smith J. A., Yanow K., 1994, *ApJ*, 432, 753
- Škoda P., Draper P. W., Neves M. C., Andrešič D., Jenness T., 2014, *Astronomy and Computing*, 7, 108
- Smith N., Gehrz R. D., Campbell R., et al., 2011, *MNRAS*, 418, 1959
- Stahl O., Leitherer C., Wolf B., Zickgraf F.-J., 1984, *A&A*, 131, L5
- Sterken C., 2011, *Information Bulletin on Variable Stars*, 6000, 1
- Surdej A., Surdej J., Swings J. P., Wamsteker W., 1981, *A&A*, 93, 285
- Swings J. P., 1974, *A&A*, 34, 333
- Torres A. F., Kraus M., Cidale L. S., et al., 2012, *MNRAS*, 427, L80
- van den Ancker, M. E., de Winter D., Tjin A Djie H. R. E., 1998, *A&A*, 330, 145
- van Genderen A. M., 2001, *A&A*, 366, 508
- van Genderen A. M., Sterken C., 1999, *A&A*, 349, 537
- van Genderen A. M., Sterken C., 2002, *A&A*, 386, 926
- van Leeuwen F., van Genderen A. M., Zegelaar I., 1998, *A&AS*, 128, 117
- Vink J. S., de Koter A., Lamers H. J. G. L. M., 1999, *A&A*, 350, 181
- Vink J. S., de Koter A., Lamers H. J. G. L. M., 2000, *A&A* 362, 295
- Zickgraf F.-J., Wolf B., Stahl O., Leitherer C., Klare G., 1985, *A&A*, 143, 421
- Zickgraf F.-J., Wolf B., Leitherer C., Appenzeller I., Stahl O., 1986, *A&A*, 163, 119
- Zickgraf F.-J., Wolf B., Stahl O., Humphreys R. M., 1989, *A&A*, 220, 206
- Zsargó J., Hillier D. J., Georgiev L. N., 2008, *A&A*, 478, 543

APPENDIX A: BASIC PROPERTIES OF STUDIED B[E] STARS, LISTS OF THE IUE OBSERVATIONS USED IN THE PAPER AND DERIVED BROAD-BAND AND LINE FLUXES, AND SUPPLEMENTARY FIGURES

Here we summarize the basic properties of studied B[e] stars.

LHA 115-S 18 The forbidden emission lines in the spectra of SMC star LHA 115-S 18 (AzV 154) were detected by [Azzopardi et al. \(1981\)](#). Besides the prominent variability of He II 4686  emission line ([Sanduleak 1978](#)) and many UV lines ([Shore et al. 1987](#)), the star also shows optical variability on different time scales ([van Genderen 2001](#), [van Genderen & Sterken 2002](#), [Clark et al. 2013](#)). A two-component model for the LHA 115-S 18 outflow consisting of fast radiatively driven wind and slow outflowing disk was proposed by [Zickgraf et al. \(1989\)](#). The star shows a strong infrared excess due to the dust ([Kastner et al. 2010](#)). The optical spectra of the star shows Raman-scattered lines ([Torres et al. 2012](#)). [Clark et al. \(2013\)](#) proposed a binary nature of the object based on the detection of X-ray emission ([Antoniou et al. 2009](#)).

LHA 115-S 65 In the case of SMC B[e] supergiant LHA 115-S 65 (CPD-75 116, RMC 50, Sk 193) any variability from IUE spectra has not been found ([Shore & Sanduleak 1984](#)). The profiles of emission lines of this star are consistent with their origin in Keplerian disk ([Kraus et al. 2010](#), [Aret et al. 2012](#)).

LHA 120-S 12 The LMC blue supergiant star LHA 120-S 12 (Sk -67 23) shows H emission and dust envelope ([Stahl et al. 1984](#)). The detected polarization signature ([Magalhes 1992](#)) points to the presence of non-spherical envelope. Measurement of ¹³C relative abundance in the infrared spectra of this star provided support for the evolved nature of the object ([Liermann et al. 2010](#)).

HD 34664 The B[e] supergiant HD 34664 (LHA 120-S 22, MWC 105) is a member of NGC 1871 association in the LMC and shows forbidden emission lines ([Fehrenbach 1971](#)). The IUE spectra of this star were studied by [Bensammar et al. \(1983\)](#). The polarimetry and spectropolarimetry revealed the existence of a disk around this star ([Magalhes 1992](#), [Schulte-Ladbeck & Clayton 1993](#)). The nebula around the supergiant, which is visible in the optical, H, and infrared wavelengths, reflects the H line of the star ([Chu et al. 2003](#)). The structure of the nebula around the star is especially complex in the IRAC observations of SPITZER.

HD 37974 The IUE spectra of the LMC B[e] supergiant HD 37974 (LHA 120-S 127) show very strong resonance lines ([Shore & Sanduleak 1984](#)). This star, which is viewed pole-on, displays signatures of the dusty disk in infrared and numerous Fe II emission lines in near-UV ([Zickgraf et al. 1985](#), [Aret et al. 2012](#)). The total mass of the dusty disk is estimated to be $3 \times 10^{-3} M_{\odot}$ from SPITZER ([Kastner et al. 2006](#)).

HD 38489 The detailed study of IUE spectra ([Shore & Sanduleak 1983](#)) of LMC supergiant HD 38489 (LHA 120-S 134) revealed presence of the stellar wind from P Cygni lines ([Shore & Sanduleak 1983](#)). [Stahl et al. \(1984\)](#) detected the infrared dust emission in the photometry of this star. Infrared observations also show a nebula around the star ([Kastner et al. 2010](#)). Some emission lines display double peaked shapes indicating their origin in rotating disk ([Aret et al. 2012](#)). The infrared spectra of the star show CO emission ([McGregor et al. 1988](#), [Oksala et al. 2013](#)).

HD 45677 Although HD 45677 (FS CMa) is classified as a B[e] star, its luminosity class is not in agreement with the supergiant characteristics ([Cidale et al. 2001](#)). The UV energy distribution shows signatures of dust absorption in HD 45677 ([Savage et al. 1978](#), [Sitko & Savage 1980](#)). The UV spectropolarimetry of this star obtained during space shuttle mission ([Schulte-Ladbeck et al. 1992](#)) revealed a bipolar reflection nebula consistent with dusty disk. [Grady et al. \(1993\)](#) interpreted available observations concluding that HD 45677 is a Herbig Be star in the phase of circumstellar material accretion. This was questioned by [Miroshnichenko \(2007\)](#), partly due to the missing pre-stellar objects in the neighborhood. The infrared properties of the star are also different from pre-main sequence objects ([Lee et al. 2016](#)). [Sitko et al. \(1994\)](#) interpreted the observed UV, optical, and infrared variability as a result of variable dust extinction. The UV flux variations show increase from MJD of about 44 000 to 48 000 discussed by [Sitko et al. \(1994\)](#). This corresponds to the recovery from a deep visual minima, that occurred around 1980 ([de Winter & van den Ancker 1997](#), [Patel et al. 2006](#)) and is accompanied by the decrease of thermal emission in infrared ([Sitko et al. 1994](#)). These variations are interpreted as a result of decreasing obscuration by circumstellar dust, which was possibly ejected after an explosive event around 1950 ([Sitko et al. 1994](#), [de Winter & van den Ancker 1997](#)).

HD 50138 The UV observations of HD 50138 (V743 Mon) star were described by [Sitko et al. \(1981\)](#). The disk of the star was resolved using spectropolarimetry ([Bjorkman et al. 1998](#)) and interferometry ([Borges Fernandes et al. 2011](#), [Ellerbroek et al. 2015](#)). The star shows complex line profile variations that were attributed to the pulsations with period significantly shorter than the rotational period of about 3.6 d ([Borges Fernandes et al. 2012](#)). The UV variability of this star was reported by [Savage et al. \(1978\)](#) based on the observations of the ANS satellite. [Hutsemekers \(1985\)](#) provide evidence of outburst in 1978–1979 from IUE line data. The photometric monitoring has not revealed a significant optical variability ([Ponomareva 1981](#), [Halbedel 1991](#)).

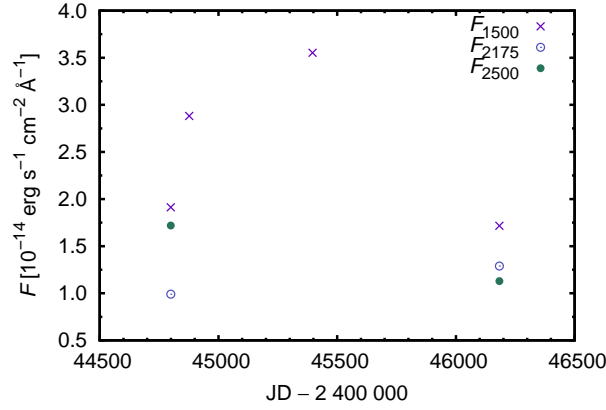


Figure A1. Variation of LHA 115-S 18 broad-band fluxes with time.

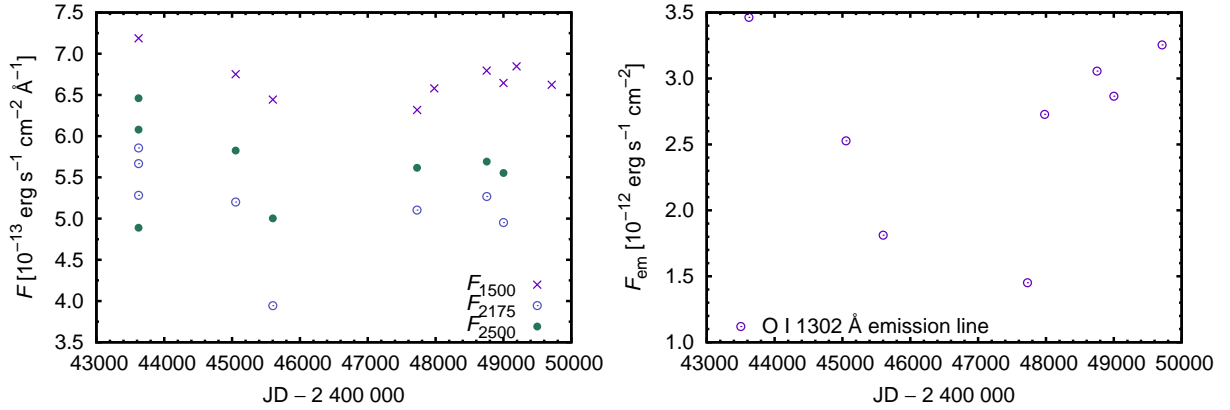


Figure A2. Variation of HD 37974 with time. *Left panel:* Broad-band fluxes. *Right panel* O I 1302 Å emission line flux.

HD 87643 The southern emission line star HD 87643 (V640 Car) is a member of a wide binary (Millour et al. 2009), resides close to the H II region RCW 47 (Crampton 1971), and is accompanied by a reflection nebula clearly visible in the optical images (Surdej et al. 1981). HD 87643 is one of the stars whose observations led to the definition of the B[e] phenomenon (Swings 1974, Allen & Swings 1976). IUE observations of HD 87643 show strong lines of Fe II (de Freitas Pacheco et al. 1982). The spectropolarimetric observations (Oudmaijer et al. 1998) revealed the existence of the disk around HD 87643. The star shows irregular light variations (Greaves 2005).

HD 94878 The eclipsing binary of β Lyrae type HD 94878 (GG Car, Marchiano et al. 2012) shows infrared excess (Allen & Swings 1976). The UV spectrum displays numerous lines of ions with low ionization potential (Brandi & Gosset 1987, Brandi et al. 1987). The polarimetric properties of the star indicate the presence of multicomponent envelope (Gnedin et al. 1992). The H α spectropolarimetry reveals the presence of the disk (Pereyra et al. 2009), which rotates with Keplerian velocity (Kraus et al. 2013). The new data from GAIA DR1 (Lindegren et al. 2016), which give the distance $r > 2$ kpc, agree with other studies (e.g., Marchiano et al. 2012) and confirm luminous nature of the source.

HD 100546 HD 100546 (KR Mus) is classified as a Herbig Ae/Be star (Hu et al. 1989). The star hosts a protoplanetary disk (Garufi et al. 2016).

HD 169515 The double-lined eclipsing binary HD 169515 (RY Sct) consists of mass losing O9.7 Ibe supergiant accompanied by massive companion (Antokhina & Kumsiashvili 1999, Grundstrom et al. 2007, Djurašević et al. 2008). The binary interaction provides a natural explanation of the H α emission line and other spectral features connected with the B[e] phenomenon. The observed ring structure of the circumstellar medium indicates possible discrete mass ejection phases (Men'shchikov & Miroshnichenko 2005, Smith et al. 2011). The IUE spectrum of HD 169515 was extensively studied by Sahade et al. (1984, 2002), who provide also identification of many UV lines.

This paper has been typeset from a $\text{\TeX}/\text{\LaTeX}$ file prepared by the author.

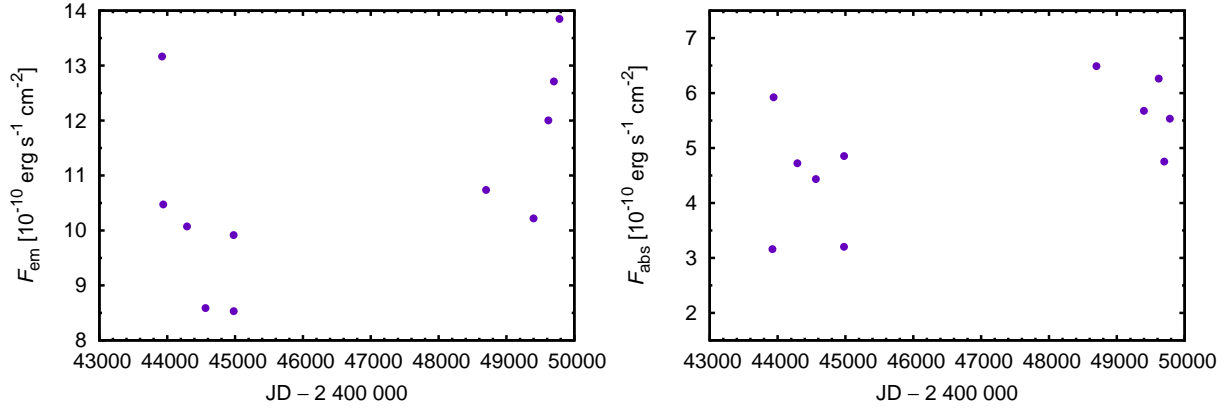


Figure A3. Variation of HD 50138 total emission line fluxes (*left panel*) and total line absorption (*right panel*) with time.

Table A1. List of the IUE observations and fluxes of LHA 115-S 18. The units of broad-band flux F_{1500} are $10^{-14} \text{ erg s}^{-1} \text{ cm}^{-2} \text{ \AA}^{-1}$, the units of broad-band fluxes F_{2175} and F_{2500} are $10^{-15} \text{ erg s}^{-1} \text{ cm}^{-2} \text{ \AA}^{-1}$. The units of F_{em} (for individual lines and the total flux) and F_{ab} (total) are $10^{-14} \text{ erg s}^{-1} \text{ cm}^{-2}$.

Camera	Image	Julian date 2,400,000.5+	F_{1500}	F_{em} N v 1245 \AA	F_{em} O I 1302 \AA	F_{em} C IV 1550 \AA	F_{em} He II 1640 \AA	F_{em} total	F_{ab}
SWP	14463	44798.59642	1.91	170	17	42	140	530	61
SWP	15122	44876.45930	2.88	240	30	88	220	680	69
SWP	19371	45395.84036	3.55	150	20	62	200	690	30
SWP	25789	46182.47697	1.72						
mean uncertainty			0.7	30	6	18	15	160	13

Camera	Image	Julian date 2,400,000.5+	F_{2175}	F_{2500}
LWR	11058	44798.64322	9.90	17.2
LWP	05836	46182.55200	12.9	11.3
mean uncertainty			12	4

Table A2. List of the IUE observations and fluxes of LHA 115-S 65. The units of broad-band flux F_{1500} are $10^{-14} \text{ erg s}^{-1} \text{ cm}^{-2} \text{ \AA}^{-1}$ and the units of broad-band fluxes F_{2175} and F_{2500} are $10^{-13} \text{ erg s}^{-1} \text{ cm}^{-2} \text{ \AA}^{-1}$.

Camera	Image	Julian date 2,400,000.5+	F_{1500}	Camera	Image	Julian date 2,400,000.5+	F_{2175}	F_{2500}
SWP	10990	44611.36670	9.97	LWR	09659	44611.38731	1.12	1.29
SWP	13503	44678.88659	9.80	LWR	10146	44678.91174	1.24	1.39
SWP	13504	44678.94138	10.6	LWR	11057	44798.54116	1.37	1.38
SWP	15121	44876.38032	10.4	LWR	11638	44876.40194	1.26	1.35
SWP	43360	48601.44294	9.77	LWP	21992	48601.73820	1.04	1.23
SWP	48257	49196.52540	11.3	LWP	26031	49196.49965	1.10	1.32
mean uncertainty				mean uncertainty			0.3	0.1

Table A3. Mean LHA 115-S 65 broad-band fluxes

Julian date 2,400,000+	F_{1500}	F_{2175}	F_{2500}
	[$10^{-13} \text{ erg s}^{-1} \text{ cm}^{-2} \text{ \AA}^{-1}$]		
44730	1.02 ± 0.04	1.25 ± 0.09	1.35 ± 0.04
48900	1.05 ± 0.13	1.07 ± 0.06	1.28 ± 0.08

Table A4. List of the IUE observations and fluxes of LHA 120-S 12. The units of broad-band flux F_{1500} are $10^{-13} \text{ erg s}^{-1} \text{ cm}^{-2} \text{ \AA}^{-1}$, units of broad-band fluxes F_{2175} and F_{2500} are $10^{-14} \text{ erg s}^{-1} \text{ cm}^{-2} \text{ \AA}^{-1}$, the units of F_{ab} (Si IV 1393 Å, C IV 1548 Å) are $10^{-12} \text{ erg s}^{-1} \text{ cm}^{-2}$, the units of F_{em} (total) are $10^{-12} \text{ erg s}^{-1} \text{ cm}^{-2}$, and the units of F_{ab} (total) are $10^{-11} \text{ erg s}^{-1} \text{ cm}^{-2}$.

Camera	Image	Julian date 2,400,000.5+	F_{1500}	F_{ab} Si IV	F_{ab} C IV	F_{em} total	F_{ab}	Camera	Image	Julian date 2,400,000.5+	F_{2175}	F_{2500}
SWP	14450	44796.80900	1.70	2.4	1.6	3.9	1.1	LWR	11639	44876.51574	10.4	8.48
SWP	36709	47727.77732	1.64	2.7	1.1	3.6	1.1	LWP	17633	47978.54468	11.0	9.59
SWP	38454	47978.52236	1.77	3.2	1.5	3.1	1.3	mean uncertainty				
SWP	38455	47978.58015	1.76		1.6	2.2	1.4				2.4	1.0
SWP	44666	48756.93182	1.72	3.6	2.2	3.0	1.3					
mean uncertainty			0.1	0.1	0.2	0.3	0.1					

Table A5. List of the IUE observations of HD 34664. The units of broad-band fluxes F_{1500} , F_{2175} , and F_{2500} are $10^{-13} \text{ erg s}^{-1} \text{ cm}^{-2} \text{ \AA}^{-1}$, the units of F_{em} (O I 1302 Å) are $10^{-13} \text{ erg s}^{-1} \text{ cm}^{-2}$, the units of F_{em} (total) are $10^{-11} \text{ erg s}^{-1} \text{ cm}^{-2}$, and the units of F_{ab} (total) are $10^{-12} \text{ erg s}^{-1} \text{ cm}^{-2}$.

Camera	Image	Julian date 2,400,000.5+	F_{1500}	F_{em} O I 1302 Å	F_{em} total	F_{ab}	Camera	Image	Julian date 2,400,000.5+	F_{2175}	F_{2500}
SWP	07634	44250.42995	2.71	9.2	2.1	2.6	LWR	06629	44250.44821	1.73	1.72
SWP	07881	44276.32969	2.74	8.2	1.9	1.3	LWR	06867	44276.30139	1.69	1.72
SWP	13505	44678.98535	2.70	11.2	1.9	1.9	LWR	06868	44276.35351	1.70	1.74
SWP	14449	44796.73076	2.75	6.5	1.8	2.0	LWR	10147	44678.99903	1.77	1.74
SWP	15114	44875.47450	2.63	7.4	1.4	3.7	LWR	11631	44875.49513	1.89	1.73
SWP	38609	47996.73495	1.42	7.6	1.2	1.4	LWP	17753	47996.70867	1.25	1.39
SWP	38667	48004.95577	1.35	9.8	1.0	1.4	LWP	17803	48004.97747	1.26	1.40
SWP	38668	48005.02173	1.39	8.4	1.1	0.8	LWP	19825	48311.47734	1.35	1.45
SWP	40926	48311.45845	1.32	8.9	1.2	0.9	LWP	21760	48577.28020	1.28	1.40
SWP	43125	48577.25947	1.30	6.5	1.0	1.1	LWP	21979	48599.49844	1.19	1.39
SWP	43349	48599.47516	1.26	9.1	1.2	1.2	LWP	21980	48599.78824	1.36	1.19
SWP	43350	48599.53042	1.25	8.2	1.0	1.2	LWP	22578	48693.92689	1.36	1.42
SWP	44160	48693.90032	1.31	7.0	1.2	0.9	LWP	23595	48831.55923	1.27	1.35
SWP	45240	48831.59244	1.35	6.2	0.9	1.4	LWP	24599	48982.92294	1.27	1.36
SWP	46592	48982.96380	1.29	5.4	1.0	1.2	LWP	26436	49252.33258	0.932	1.07
SWP	48202	49190.30118	0.995	5.2	0.8	0.8	LWP	28072	49479.38554	1.33	1.44
SWP	48709	49253.41809	1.05	5.3	1.0	1.3	LWP	29749	49710.25362	1.27	1.38
SWP	50703	49478.58207	1.30	6.2	1.0	0.9	mean uncertainty				
SWP	50711	49479.43130	1.36	5.9	1.0	1.0				0.3	0.1
SWP	53169	49710.28760	1.12	5.6	0.9	1.3					
SWP	54482	49829.01160	1.30	5.8	0.9	0.9					
mean uncertainty			0.1	1.2	0.1	0.2					

Table A6. List of the IUE observations of HD 37974. The units of broad-band fluxes F_{1500} , F_{2175} , and F_{2500} are $10^{-13} \text{ erg s}^{-1} \text{ cm}^{-2} \text{ \AA}^{-1}$, the units of F_{em} (O I 1302 Å) are $10^{-12} \text{ erg s}^{-1} \text{ cm}^{-2}$, the units of F_{em} (total) are $10^{-11} \text{ erg s}^{-1} \text{ cm}^{-2}$, and the units of F_{ab} (total) are $10^{-11} \text{ erg s}^{-1} \text{ cm}^{-2}$. We have not used LWP spectra 17752 and 26022 for our analysis, because their flux around 2000 Å does not correspond to the SWP spectra taken roughly at the same time.

Camera	Image	Julian date 2,400,000.5+	F_{1500}	F_{em} O I 1302 Å	F_{em} total	F_{ab}	Camera	Image	Julian date 2,400,000.5+	F_{2175}	F_{2500}
SWP	01402	43620.84477	7.19	3.5	3.1	2.8	LWR	01364	43620.77220	5.28	4.89
SWP	16617	45052.96092	6.75	2.5	2.4	2.4	LWR	01365	43620.81664	5.67	6.46
SWP	21142	45600.65824	6.44	1.8	2.2	2.3	LWR	01366	43620.88505	5.86	6.08
SWP	36705	47726.43124	6.32	1.5	2.0	2.2	LWP	02005	45600.74598	3.94	5.00
SWP	38466	47979.76919	6.58	2.7	2.3	2.3	LWR	12854	45052.94009	5.20	5.83
SWP	44640	48752.84347	6.79	3.1	2.6	2.4	LWP	15959	47726.40155	5.10	5.62
SWP	46715	48999.78725	6.65	2.9	2.6	2.1	LWP	23083	48752.87841	5.27	5.69
SWP	48224	49192.51418	6.85				LWP	24721	48999.80857	4.95	5.55
SWP	53170	49710.35884	6.62	3.3	2.7	2.0					
mean uncertainty			0.4	0.6	0.2	0.2	mean uncertainty			0.8	0.5

Table A7. List of the IUE observations of HD 38489. The units of broad-band fluxes F_{1500} , F_{2175} , and F_{2500} are $10^{-13} \text{ erg s}^{-1} \text{ cm}^{-2} \text{ \AA}^{-1}$, the units of F_{em} (He II 1640 Å, O III 1665 Å, and N III 1752 Å) are $10^{-12} \text{ erg s}^{-1} \text{ cm}^{-2}$, the units of F_{em} (total) are $10^{-11} \text{ erg s}^{-1} \text{ cm}^{-2}$, and the units of F_{ab} (total) are $10^{-12} \text{ erg s}^{-1} \text{ cm}^{-2}$.

Camera	Image	Julian date 2,400,000.5+	F_{1500}	F_{em} He II 1640 Å	F_{em} O III 1665 Å	F_{em} N III 1752 Å	F_{em} total	F_{ab}
SWP	14447	44796.61089	3.00	1.1	2.8	3.1	2.0	4.2
SWP	15117	44875.62457	3.02	1.0	2.0	3.1	1.5	4.8
SWP	25790	46182.62654	2.93	0.97	1.8	2.4	1.7	4.5
SWP	38464	47979.62427	2.91	1.7	2.5	2.5	1.9	4.7
SWP	44163	48694.08735	2.86	1.5	2.6	2.9	2.0	3.0
SWP	46714	48999.73408	3.06	1.7	2.3	3.0	2.2	3.3
SWP	48223	49192.46020	3.06	1.3	2.4	3.1	2.0	4.4
mean uncertainty			0.2	0.4	0.3	0.4	0.2	0.4

Camera	Image	Julian date 2,400,000.5+	F_{2175}	F_{2500}
LWR	11047	44796.58758	1.47	1.67
LWR	11634	44875.64559	1.52	1.73
LWP	17644	47979.64906	1.47	1.69
LWP	22580	48694.05967	1.47	1.68
LWP	22581	48694.11313	1.50	1.74
LWP	24720	48999.75894	1.51	1.70
LWP	25987	49192.47408	1.52	1.70
mean uncertainty			0.4	0.2

Table A8. List of the IUE observations of HD 45677. The units of broad-band fluxes F_{1500} , F_{2175} , and F_{2500} are 10^{-12} erg s $^{-1}$ cm $^{-2}$ Å $^{-1}$, the units of F_{em} (O I 1641 Å) are 10^{-12} erg s $^{-1}$ cm $^{-2}$, the units of F_{em} (N I 1745 Å) are 10^{-11} erg s $^{-1}$ cm $^{-2}$, and the units of F_{em} (total) and F_{ab} (total) are 10^{-10} erg s $^{-1}$ cm $^{-2}$.

Camera	Image	Julian date 2,400,000.5+	F_{1500}	F_{em} O I	F_{em} N I	F_{em} total	F_{ab}	Camera	Image	Julian date 2,400,000.5+	F_{2175}	F_{2500}
SWP	01388	43617.91900	7.98					LWR	01342	43617.86552	3.88	4.43
SWP	02707	43771.73863	8.62					LWR	01343	43617.95139	3.85	4.48
SWP	02772	43777.64468	8.86					LWR	02416	43771.69562	4.08	4.77
SWP	04340	43926.86856			1.5	2.4	1.8	LWR	02467	43777.63777	4.19	5.09
SWP	04761	43959.28757			1.4	2.6	1.6	LWR	05630	44135.58619	3.87	4.67
SWP	06569	44135.58933	7.78					LWR	06966	44290.98922	3.69	4.46
SWP	08006	44290.99348	8.14					LWR	09357	44564.23236	4.00	4.51
SWP	10648	44564.23906	8.18					LWR	09850	44639.18781	3.73	4.65
SWP	10652	44564.46919		20	1.2	2.6	1.1	LWR	12309	44978.12974	4.28	4.86
SWP	11230	44639.19581	8.14					LWP	22428	48673.16886	6.37	5.92
SWP	15991	44978.02437		14	1.3	3.2	1.4	LWP	22467	48679.00908	6.29	7.14
SWP	15992	44978.12183	8.86					LWP	24554	48978.34880	6.11	6.83
SWP	40272	48230.26057		24	1.6	3.6	1.9	LWP	27420	49397.98586	5.81	6.57
SWP	44033	48673.17445	14.4					LWP	29140	49605.39065	5.93	6.22
SWP	44069	48679.02518	13.6					LWP	31508	49980.39867	5.82	6.79
SWP	46547	48978.12535		28	1.9	3.9	2.2					
SWP	46548	48978.23332		33	1.5	4.1	2.1	mean uncertainty				
SWP	46549	48978.34512	12.7					0.7				
SWP	48869	49268.38414		34	1.7	4.8	1.8	0.4				
SWP	50020	49397.96430		40	1.7	5.6	2.0					
SWP	50021	49398.00809	12.5									
SWP	50042	49400.11357	11.6									
SWP	52074	49605.35304		33	2.0	4.7	2.2					
SWP	52075	49605.40010	12.6									
SWP	53046	49698.45771		47	1.9	4.8	3.1					
SWP	55972	49980.35381		35	1.5	3.7	1.9					
SWP	55973	49980.40276	13.5									
mean uncertainty			0.5	1.8	0.2	0.2	0.1					

Table A9. List of the IUE observations of HD 50138. The units of broad-band fluxes F_{1500} , F_{2175} , and F_{2500} are 10^{-11} erg s $^{-1}$ cm $^{-2}$ Å $^{-1}$, the units of F_{em} (1530 Å) are 10^{-11} erg s $^{-1}$ cm $^{-2}$, and the units of F_{em} and F_{ab} (total) are 10^{-10} erg s $^{-1}$ cm $^{-2}$.

Camera	Image	Julian date 2,400,000.5+	F_{1500}	F_{em} 1530 Å	F_{em} total	F_{ab}	Camera	Image	Julian date 2,400,000.5+	F_{2175}	F_{2500}
SWP	03663	43863.62772	2.19				LWR	02499	43780.64124	1.50	1.26
SWP	04294	43922.93508	1.92				LWR	03226	43863.52685	1.35	1.11
SWP	04295	43923.02686	1.81	4.9	13.2	3.2	LWR	03247	43865.44774	1.44	1.31
SWP	04557	43941.29904	2.36	5.8	10.5	5.9	LWR	03794	43922.92648	1.17	1.04
SWP	04947	43978.87895	2.40				LWR	03796	43923.00149	1.17	1.05
SWP	08007	44291.06204	2.08	3.2	10.1	4.7	LWR	03967	43941.27313	1.47	1.24
SWP	08008	44291.10022	2.20				LWR	04276	43978.86907	1.37	1.14
SWP	10649	44564.30298	1.40	4.1	8.6	4.4	LWR	06958	44289.23593	1.09	0.847
SWP	10650	44564.33850	1.46				LWR	06967	44291.02461	1.09	0.929
SWP	11231	44639.24050	1.83				LWR	06968	44291.09541	1.21	0.985
SWP	15993	44978.17375	1.75	2.9	9.9	3.2	LWR	09358	44564.27408	0.585	0.574
SWP	15994	44978.22819	1.89				LWR	09359	44564.33405	0.789	0.680
SWP	16017	44980.17490	1.80	3.3	8.5	4.9	LWR	09851	44639.23849	0.908	0.724
SWP	44190	48699.66053	1.88	4.7	10.7	6.5	LWR	12310	44978.19663	0.814	0.738
SWP	50022	49398.06495	2.81				LWR	12311	44978.23478	0.962	0.821
SWP	50023	49398.12977	2.61	4.1	10.2	5.7	LWR	12322	44980.15007	0.894	0.740
SWP	50024	49398.16796	2.87				LWP	21563	48559.04685	0.980	0.801
SWP	52169	49616.47446	2.62	9.0	12.0	6.3	LWP	22631	48699.68528	1.02	0.824
SWP	53047	49698.53272	2.25	6.3	12.7	4.8	LWP	27421	49398.06091	1.50	1.37
SWP	54035	49780.85206	2.10	4.4	13.8	5.5	LWP	27422	49398.09727	1.46	1.26
mean uncertainty			0.09	0.5	0.5	0.2	LWP	27423	49398.14733	1.53	1.33
							LWP	27430	49400.06514	1.33	1.19
							LWP	29213	49616.44913	1.43	1.11
							LWP	29691	49698.49794	1.24	1.12
							LWP	30154	49780.82694	1.19	1.01
							LWP	30212	49787.84814	0.995	0.942
							LWP	30215	49788.91653	1.09	0.989
							LWP	30230	49790.05439	1.19	0.986
							LWP	30236	49791.10010	1.22	1.01
							LWP	30243	49792.04370	1.28	1.07
							LWP	30248	49792.82657	1.13	0.942
							LWP	30251	49793.82873	1.02	0.880
							LWP	30256	49794.95347	1.15	1.04
							LWP	30261	49795.81162	1.17	1.01
							LWP	30268	49796.82841	1.32	1.06
							LWP	30280	49797.91027	1.20	1.08
							LWP	30290	49799.10282	1.46	1.26
							LWP	30297	49800.10454	1.21	0.970
							LWP	30299	49800.93271	1.16	0.933
							LWP	30305	49801.80813	1.30	1.06
							LWP	30311	49802.83435	1.35	1.10
							LWP	30316	49803.82211	1.24	1.06
mean uncertainty									0.2	0.07	

Table A10. List of the IUE observations of HD 87643. The units of broad-band fluxes F_{1500} , F_{2175} , and F_{2500} are $10^{-13} \text{ erg s}^{-1} \text{ cm}^{-2} \text{ \AA}^{-1}$, the units of $F_{\text{em}} (1730 \text{ \AA})$ are $10^{-12} \text{ erg s}^{-1} \text{ cm}^{-2}$, the units of $F_{\text{em}} (\text{total})$ are $10^{-11} \text{ erg s}^{-1} \text{ cm}^{-2}$, and $F_{\text{ab}} (\text{total})$ are $10^{-12} \text{ erg s}^{-1} \text{ cm}^{-2}$.

Camera	Image	Julian date 2,400,000.5+	F_{1500}	F_{em} 1730 \AA	F_{em} total	F_{ab}	Camera	Image	Julian date 2,400,000.5+	F_{2175}	F_{2500}
SWP	05838	44071.98731	3.56	2.9	5.0	2.9	LWR	05084	44071.96524	0.990	1.83
SWP	05889	44076.10701	3.53	3.0	4.2	7.7	LWR	05085	44072.00495	1.00	1.87
SWP	09166	44391.17960	3.83				LWR	05144	44076.09434	1.12	1.91
SWP	13760	44714.20766	3.48	2.6	4.3	3.5	LWP	06038	46208.60380	0.933	2.20
SWP	25996	46208.58548	3.07	2.4	3.5	3.1	LWP	06098	46216.40606	0.911	2.30
SWP	26040	46216.42460	3.54	2.5	4.0	4.8	LWP	08199	46564.80108	0.697	1.39
SWP	28309	46564.78045	2.43	2.6	4.2	4.8	LWR	10392	44714.19108	1.13	2.68
SWP	36803	47744.58941	4.01	2.4	4.3	6.1	LWR	10393	44714.31543	1.27	2.94
SWP	46913	49029.08163	3.09	2.2	3.4	5.2	LWP	16078	47744.57379	0.938	2.54
SWP	50710	49479.33012	2.21	1.9	2.4	5.0	LWP	20595	48421.32603	0.298	1.18
SWP	53842	49754.11026	2.17	2.1	2.5	4.6	LWP	24888	49028.92607	0.601	2.30
mean uncertainty			0.2	0.3	0.4	0.5	LWP	24890	49029.17346	0.705	1.87
							LWP	26086	49204.77187	0.596	1.68
							LWP	26143	49213.18713	0.739	1.79
							mean uncertainty		0.9	0.3	

Table A11. List of the IUE observations of HD 94878. The units of broad-band fluxes F_{1500} , F_{2175} , and F_{2500} are $10^{-13} \text{ erg s}^{-1} \text{ cm}^{-2} \text{ \AA}^{-1}$, the units of $F_{\text{ab}} (\text{C II } 1335 \text{ \AA} \text{ and C IV } 1548 \text{ \AA})$ are $10^{-12} \text{ erg s}^{-1} \text{ cm}^{-2}$, the units of F_{em} and $F_{\text{ab}} (\text{total})$ are $10^{-11} \text{ erg s}^{-1} \text{ cm}^{-2}$.

Camera	Image	Julian date 2,400,000.5+	F_{1500}	F_{ab} C II	F_{ab} C IV	F_{em}	F_{ab} total	Camera	Image	Julian date 2,400,000.5+	F_{2175}	F_{2500}
SWP	02685	43769.84366	19.4		9.2			LWR	02396	43769.77632	5.41	9.75
SWP	02686	43769.89388	24.2	8.8	9.6	7.1	7.2	LWR	02397	43769.86043	4.92	12.1
SWP	05679	44054.14513	26.5	3.5	13	4.9	8.8	LWR	04921	44054.11469	5.09	12.5
SWP	06737	44149.71582	21.2	3.3	7.8	3.4	6.5	LWR	07683	44365.30913	3.69	8.75
SWP	08936	44365.16023	19.6					LWR	08071	44408.88296	5.41	10.9
SWP	09309	44408.86859	26.1	7.2	11	4.3	7.3	LWR	14625	45287.68397	4.27	9.09
SWP	18555	45287.70249	23.1	7.4	12	3.7	8.1	mean uncertainty		1.2	1.0	
mean uncertainty			1.1	1.6	2	0.3	0.5					

Table A12. List of the IUE observations of HD 100546. The units of broad-band fluxes F_{1500} , F_{2175} , and F_{2500} are 10^{-11} erg s $^{-1}$ cm $^{-2}$ Å $^{-1}$, the units of F_{ab} (C II 1335 Å and Fe II 1657 Å) are 10^{-11} erg s $^{-1}$ cm $^{-2}$, the units of F_{em} (1779 Å + 1784 Å) are 10^{-11} erg s $^{-1}$ cm $^{-2}$, and the units of F_{em} and F_{ab} (total) are 10^{-10} erg s $^{-1}$ cm $^{-2}$.

Camera	Image	Julian date 2,400,000.5+	F_{1500}	F_{ab} C II	F_{ab} Fe II	F_{em} 1779 Å+	F_{em} total	F_{ab}
SWP	39712	48160.68056	2.15	5.2	1.9	0.76	1.9	4.5
SWP	47481	49091.17277	2.07	5.1	0.75	0.96	2.6	3.1
SWP	54065	49783.82326	2.05	5.4	3.1	1.1	2.7	5.0
SWP	54658	49849.02155	2.26					
SWP	54753	49862.71465	2.38					
SWP	54754	49862.79287	2.18	5.1	1.2	1.2	3.4	3.3
mean uncertainty			0.07	0.5	0.3	0.5	0.1	0.2

Camera	Image	Julian date 2,400,000.5+	F_{2175}	F_{2500}
LWP	16052	47740.75450	1.06	0.913
LWP	16075	47744.03140	1.06	0.904
LWP	30679	49849.01533	1.14	1.00
LWP	30770	49862.70994	1.12	0.959
LWP	30771	49862.76354	0.984	0.842
mean uncertainty			0.2	0.06

Table A13. List of the IUE observations of HD 169515. The units of broad-band fluxes F_{1500} , F_{2175} , and F_{2500} are 10^{-14} erg s $^{-1}$ cm $^{-2}$ Å $^{-1}$, the units of F_{em} (C IV 1550 Å) are 10^{-13} erg s $^{-1}$ cm $^{-2}$, the units of F_{ab} (Fe II 1658 Å) are 10^{-13} erg s $^{-1}$ cm $^{-2}$, and the units of F_{em} and F_{ab} (total) are 10^{-12} erg s $^{-1}$ cm $^{-2}$.

Camera	Image	Julian date 2,400,000.5+	F_{1500}	F_{em} C IV	F_{ab} Fe II	F_{em} total	F_{ab}	Camera	Image	Julian date 2,400,000.5+	F_{2175}	F_{2500}
SWP	01543	43642.75860	8.14	3.0	2.3	10.2	5.1	LWR	01493	43642.72896	0.706	5.30
SWP	05830	44071.39234	8.71	4.8	0.9	4.9	2.6	LWR	05078	44071.38159	0.172	6.19
SWP	05831	44071.47761	10.6	4.6	1.0	6.3	2.6	LWR	05079	44071.41798	0.456	6.68
SWP	06614	44139.72653	13.0	7.7	3.1	4.4	2.5	LWR	05672	44139.69677	0.594	8.16
SWP	08938	44365.53453	7.90	6.9	1.4	3.4	1.0	LWR	05673	44139.74953	0.528	8.02
SWP	17386	45159.00706	12.7	8.9	2.8	4.5	1.7	LWR	07686	44365.56572	0.175	4.51
SWP	17408	45161.95042	10.5	5.9	2.2	2.3	2.0	LWP	13161	47283.80280	0.753	8.02
SWP	18099	45236.89806	12.4	6.2	2.9	3.4	2.4	LWR	13636	45158.93463	0.572	7.52
SWP	33431	47283.76895	13.0	5.7	2.7	3.0	2.1	LWR	13658	45161.90118	0.426	6.30
mean uncertainty			1.5	3	0.9	0.6	0.3	LWR	13659	45161.99969	0.634	6.56
								LWR	14249	45236.92795	0.643	7.63
								mean uncertainty			1.7	1.2